Dalton Transactions

ROYAL SOCIETY OF CHEMISTRY

PAPER

View Article Online
View Journal | View Issue

Cite this: *Dalton Trans.*, 2024, **53**, 14028

Nitrogen-enriched flexible metal–organic framework for CO_2 adsorption†

Andrés Lancheros, *[a,b,c] Subhadip Goswami, [c] Ximena Zarate,[d] Eduardo Schott *[a,b] and Joseph T. Hupp [c]

Received 17th May 2024,
Accepted 25th July 2024

DOI: 10.1039/d4dt01457j

rsc.li/dalton

A novel MOF named $[Zn_2(L)(DMF)]$ was synthesized using solvothermal methods from the reaction of the new linker (4,4′,4′′-(4,4′,4′′-(benzene-1,3,5-triyltris(methylene))tris(3,5-dimethyl-1*H*-pyrazole-4,1-diyl))tribenzoic acid) and $Zn(NO_3)_2 \cdot 6H_2O$. This new MOF was characterized by means of different techniques: powder X-ray diffraction, N_2 adsorption and desorption isotherms, thermogravimetric analysis, and scanning electron microscopy. Furthermore, suitable crystals were obtained, which allowed us to perform the X-Ray structure determination of this MOF. The capability of these new MOF to adsorb CO_2 at different temperatures was measured and its isosteric enthalpy of adsorption was calculated. The novel MOF shows an uncommon node composed of a $Zn_3(–COO)_6(DMF)_2$, and the asymmetric unit contains one crystallographically independent linker, one DMF molecule, and two Zn atoms. The $[Zn_2(L)(DMF)]$ MOF is a microporous material with high crystallinity and stability up to 250 °C. The multiple nitrogenated pyrazole linkers in its framework enhance its CO_2 adsorption capabilities. This material exhibits a low CO_2 isosteric enthalpy of adsorption (H_{ads}), comparable to previously reported values for similar nitrogenated materials. All the observed CO_2 adsorption capacities were further supported by DFT calculations.

Introduction

The increase in greenhouse gas emissions into the atmosphere, mainly from burning fossil fuels, particularly carbon dioxide (CO_2), has been ascribed to the rise in world temperatures. The primary sources of industrial pollution are plants that produce cement, steel, and coal-fired electricity.[1–3] The most popular and established process for CO_2 capture in those industries is post-combustion gas absorption, performed using aqueous solutions of amino alcohols, such as monoethanolamine (MEA) or diethanolamine (DEA).[4–7] However, its regeneration requires high energy consumption, can cause equipment corrosion, and may reduce its effectiveness due to amine degradation.[7–9]

Lately, coordination polymers and Metal–Organic Frameworks (MOF) have been recognized as some of the most promising alternatives for CO_2 adsorption.[10] MOFs are a class of crystalline porous materials based on metal ions (nodes) coordinated with organic ligands that form ordered and specific structures.[11–14] They are characterized by their enormous internal surface area, which can be up to 10 000 m^2 g^{-1}; ultraporosity, up to 90% of free volume, in nanometer-sized cavities or open channels; low densities, for example, 0.126 g cm^{-3},[15] uniform spatial dispersion of components; tunable pore sizes; tunable topologies, hybrid organic–inorganic nature, and multi-functionality.[16] The adsorption capacity of MOFs is mainly related to the surface area, but pressure and adsorption temperature play a vital role in the interaction with the adsorbent.[3]

To improve CO_2 adsorption capacity and selectivity using MOFs, two strategies have been widely reported: (1) incorporation of coordinately unsaturated metal sites. These sites on the structure favor the immobilization of CO_2 molecules by inducing dipole–quadrupole interactions. The interaction between the Lewis acid sites of the metal with CO_2 molecules is favored, providing high adsorption at very low pressures and selectivity of CO_2 over N_2.[17,18] (2) Decoration with basic Lewis sites. As CO_2 molecules have quadrupole moments, the presence of polar groups in MOFs improves the adsorption of CO_2 and the selectivity concerning gases such as CH_4, N_2, and H_2 (non-polar).[3] The incorporation or functionalization of organic

---

[a] *Department of Inorganic Chemistry, Faculty of Chemistry and Pharmacy, UC Energy Center, Center for Research in Nanotechnology and Advanced Materials (CIEN-UC), Pontificia Universidad Católica de Chile, Av. Vicuña Mackenna 4860, Santiago, Chile. E-mail: aflancheros@uc.cl, maschotte@gmail.com*

[b] *ANID – Millennium Science Initiative Program – Millennium Nuclei on Catalytic Process Towards Sustainable Chemistry (CSC), Chile*

[c] *Department of Chemistry and International Institute for Nanotechnology, Northwestern University, 2145 Sheridan Road, Evanston, Illinois 60208, USA*

[d] *Institute of Applied Sciences, Faculty of Engineering, Universidad Autónoma de Chile, Av. Pedro de Valdivia 425, Santiago, Chile*

† Electronic supplementary information (ESI) available. CCDC 2355199. For ESI and crystallographic data in CIF or other electronic format see DOI: **https://doi.org/10.1039/d4dt01457j**

molecules with polar groups capable of interacting strongly with CO_2 can occur in the MOF's nodes or ligands. Examples of these groups are amine, phosphonate, and sulfonate. Amines are most generally studied due to their high affinity towards CO_2 molecules and selectivity. Among them are primary, secondary, or tertiary amines, tetrazole, triazine, imidazole, and pyrazole, among others.[19–21]

The herein study synthesizes and characterizes a novel Zn(II) MOF using an innovative, flexible pyrazole carboxylate linker. The carboxylic acid moiety in the linker structure will play a key role in developing the three-dimensional structure, while unbound pyrazoles will enable nitrogen sites to bind with CO_2 molecules. Additionally, we aim to investigate the potential generation of Lewis acid sites within the MOF nodes through the desorption of coordinated solvent molecules on the node after activation. Also, the enthalpy of adsorption (ΔH_{ads}) by the Clausius Clapeyron equation was modeled at different temperatures. Finally, to explore the MOF–CO_2 interaction, DFT calculations over the interacting structure were performed.

Experimental section

Materials

All reagents and solvents were commercially purchased from commercial suppliers and used as received without further purification. 1,3,5-tris(bromomethyl)benzene (97%), acetylacetone (≥99%), acetone (≥97%), benzene (99.8%), hexane (95%), magnesium sulfate anhydrous (≥98%), potassium (98%), potassium iodide (≥99%), *tert*-butyl alcohol (≥99.5%) and tetrahydrofuran (99.9%) were purchased from Sigma Aldrich. 4-Hydrazinobenzoic acid (97%) was purchased from Fisher Chemical. *N*,*N*-Dimethylformamide (DMF) (99%) was purchased from Acros organics, and zinc(II) nitrate hexahydrate (98%) was purchased from Strem Chemicals.

Synthesis of the linker

The linker, whose structure is shown in Fig. 1, was synthesized in a two-step synthetical procedure. An intermediate tris-β diketonic was produced according to a previous report,[22] where the 1,3,5-tris (bromomethyl) benzene reacted with potassium *tert*-butoxide and acetylacetone. Then, this compound reacted with 4-hydrazinobenzoic acid to obtain the final linker. Detailed synthetic procedures and structural characterizations of the precursor and linker are provided in the ESI (Scheme S1 and Fig. S1–S16†).

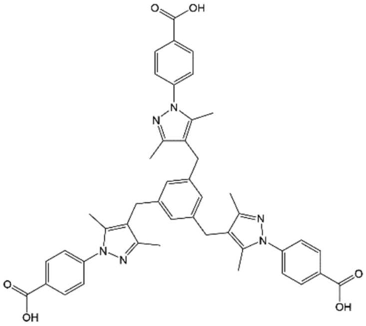

Fig. 1 Chemical structure of the novel linker.

Synthesis of [Zn_2(L)DMF] single crystal

In a 3-dram vial, the linker (190.60 mg, 0.25 mmol, 1 equiv.) was dissolved in *N*,*N*′-dimethylformamide (DMF) (8.0 mL) using an ultrasonic water bath. Meanwhile, in another 3-dram vial, $Zn(NO_3)_2 \cdot 6H_2O$ (47.30 mg, 0.16 mmol, 0,6 equiv.) was also dissolved in DMF (8.0 mL). Both solutions were mixed in a 6-dram vial, capped, and placed in an oven preheated to 100 °C for 48 hours. After cooling down to room temperature, the product was obtained by centrifugation at 8500 rpm for 10 minutes. The solid was washed three times with DMF (10 mL) and three times with acetone (10 mL) every two hours. Finally, it was soaked with acetone overnight, centrifuged, and dried in air to give a light-yellow powder.

Physical measurements

Single-crystal X-ray crystallography. A suitable crystal was selected and mounted on a glass fiber with Paratone oil on a XtaLAB Synergy, single source at offset/far, HyPix diffractometer. During data collection, the crystal was kept at 100 K. The structure was solved using Olex2[23] with the ShelXT[24] structure solution program using intrinsic phasing and refined with the XL[25] refinement package using least squares minimization. The refinement result is summarized in Table S1.† Crystallographic data for the [Zn_2(L)DMF] structure in CIF format has been deposited in the Cambridge Crystallographic Data Centre (CCDC) under deposition numbers CCDC 2355199.†

Powder X-ray diffraction (PXRD). PXRD patterns were recorded on a STOE-STADIMP powder diffractometer equipped with an asymmetrically curved Germanium monochromator (CuKα1 radiation, λ = 1.54056 Å) and a one-dimensional silicon strip detector (MYTHEN2 1K from DECTRIS) at room temperature on the IMSERC X-ray Facility at Northwestern University. The line-focused Cu X-ray tube was operated at 40 kV and 40 mA. The activated MOF powder was packed in a 3 mm metallic mask, sandwiched between two polyimide layers of tape, and measured in transmission geometry in a rotating holder. Intensity data from 1 to 34 degrees 2θ were collected over 7 minutes. The instrument was calibrated against a NIST Silicon standard (640d) prior to the measurement.

N_2 adsorption and desorption isotherms. Before each analysis, samples were thermally treated at 120 °C for 16 h under a high vacuum on a Smart VacPrep from Micromeritics. Then, using the Micromeritics Tristar II 3020 (Micromeritics, Norcross, GA) N_2 adsorption and desorption isotherms were measured at 77 K and pore-size distributions were obtained from density functional theory (DFT). Around 50 mg of sample was used in each measurement and Brunauer–Emmett–Teller (BET) surface area was calculated in the region P/P_0 = 0.005–0.05.

Thermogravimetric analysis (TGA). The TGA measurement was performed on a TGA/DCS 1 system (Mettler-Toledo AG, Schwerzenbach, Switzerland), which runs on a PC with STARe software. Samples were heated from 25 to 600 °C at 10 °C min^{-1} under nitrogen with a flow rate of 20 mL min^{-1}.

Scanning electron microscopy (SEM). Before imaging, the samples were coated with OsO_4 to ~9 nm thickness in a Denton Desk III TSC Sputter Coater. SEM images were collected on a Hitachi SU8030 FE-SEM (Dallas, TX) microscope.

CO_2 sorption measurements. Before analyses, the sample was activated by heating 120 °C under dynamic vacuum on a Smart Vacprep from Micromeritics until the outgassing rate was <5 μmHg min^{-1} using a mass of approximately 50 mg. Then, CO_2 adsorption experiments were performed by using Micromeritics ASAP 2020 surface area analyzer. The isotherms were measured around standard conditions at 273 K, 288 K, and 298 K from 0 to 800 mbar (0–80 kPa). The experiment temperatures were maintained employing a Micromeritics Iso Controller. The Clausius–Clapeyron equation (eqn (1)) was used to calculate the isosteric enthalpy of CO_2 adsorption (ΔH_{ads}, kJ mol^{-1}).[26]

$$\Delta H_{\text{ads}}\,(n) = -R \cdot \ln\left(\frac{p_2}{p_1}\right)\frac{T_1 \cdot T_2}{(T_2 - T_1)} \tag{1}$$

where p is pressure, T is temperature, and R is the ideal gas constant (8.314 J mol^{-1} K^{-1}).

Theoretical calculations

Density functional theory calculations in the scalar relativistic framework were carried out using the ADF 2019.01 code[27,28] with the ZORA Hamiltonian.[29–31] Triple-ξ Slater basis set (STO-TZP) for valence electrons was employed[32] with the functional RPBE[33] including dispersion correction (Grimme D3).[34] Using Versluis and Ziegler's analytical energy gradient method, no symmetry restraints were considered for the equilibrium geometries.[35] The nature of the binding interaction was studied in the representation of the MOF simplified pore model with different amounts of CO_2 molecules through the Morokuma–Ziegler decomposition scheme. In this scheme, the binding energy is determined by applying a fragmentation of the molecular structure, which allows the decomposition of the interaction energy (ΔE_{Int}) among the fragments. Therefore, this compound was studied as two fragments constituting the system: the MOF pore simplified model and the surrounding CO_2 molecules (considering from 2 up to 8 CO_2 molecules interacting with the MOF). The interaction energy can be decomposed as:[36]

$$\Delta E_{\text{Int}} = \Delta E_{\text{Pauli}} + \Delta E_{\text{Elec}} + \Delta E_{\text{Orb}} + \Delta E_{\text{Disp}} \tag{2}$$

The ΔE_{Pauli} refers to the Pauli repulsion (exchange repulsion). This energy is responsible for any steric repulsion. The remaining three terms correspond to the classical electrostatic interaction (ΔE_{Elec}), the dispersive contribution (ΔE_{Disp}), and the effect of the orbital interaction and polarization effects (ΔE_{Orb}). All these terms have a stabilizing contribution to the interaction energy.

Results and discussion

After activation and washing, the novel $[Zn_2(L)(DMF)]$ MOF is a fine white powder with light-marron crystals (Fig. S17b†). The SEM picture (Fig. S17c†) depicts the particle distribution as irregularly formed clusters with an average particle size ranging from 10 to 100 μm.

Crystal structure analysis

The synthesized MOF structure was elucidated by single-crystal X-ray diffraction (XRD) (Table S1†). The analysis revealed that $[Zn_2(L)DMF]$ crystallizes in the monoclinic $P21/n$ space group. The asymmetric unit of $[Zn_2(L)DMF]$ contains one crystallographically independent linker, one DMF molecule, and two Zn(II) atoms (Fig. 2a). Also, it showed that the framework is composed of a $Zn_3(-COO)_6(DMF)_2$ node (Fig. 2b). The central Zn(II) shows octahedral coordination with carboxylate oxygen atoms, and the other two Zn(II) show distorted trigonal bipyramidal geometry coordinated to four carboxylate linkers (Fig. 2c). The remaining positions are bound to the oxygen of a DMF molecule, which was used as a solvent in the reaction. This uncommon type of node has already been reported for the MOF $Zn_3(BDC)_3 \cdot 6CH_3OH$ (BDC: 1,4-benzenedicarboxylate).[37,38]

The central octahedral structure in the node's MOF shows no distortion, and the angles correspond to the theoretical ones, 90° for each measured angle. However, the trigonal bipyramidal structures are not in the equatorial position (as the O–Zn–O angles should be 120°), showing distorted angles with values of 104.29°, 117.46°, and 133.81°. On the other hand, the angles O–Zn–O between the equatorial and axial oxygen should have a value of 90°; however, as shown in Fig. S18d,† the structure is distorted and no 90° angles were

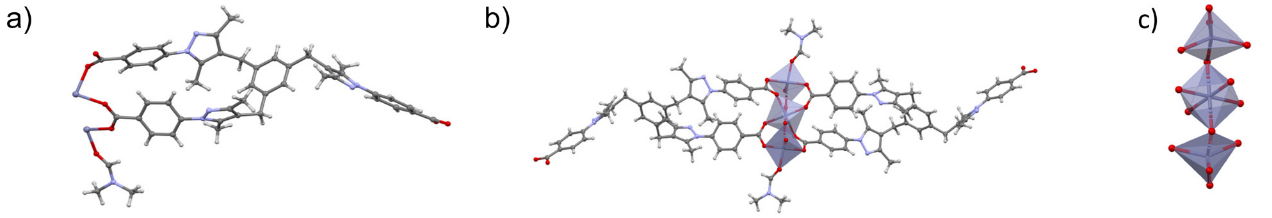

Fig. 2 For $[Zn_2(L)(DMF)]$, (a) asymmetric unit, (b) coordination environment for Zn^{2+}, (c) node structure.

found (Fig. S18a†). This distortion is attributed to the central octahedron's stability and the linker's rigidity. Each linker connects six Zn^{2+} ions, resulting in a three-dimensional (3D) porous (not interpenetrated) network due to its flexibility (Fig. 3). Removing the weak bound DMF molecules by activation offers an opportunity to achieve a porous material with unsaturated zinc centers, which may benefit CO_2 adsorption.[39] Zn–O bond lengths ranged from 1.948 to 2.293 Å. These values are consistent with those previously reported for Zn(II)-based MOFs.[37,40–42]

Powder X-ray diffraction (PXRD) and thermogravimetric analysis (TGA)

The structural stability of $[Zn_2(L)DMF]$ sample was confirmed by the sharp and clear diffraction peaks in PXRD patterns after activation under dynamic vacuum at 120 °C for 16 h, activation by supercritical CO_2, and after CO_2 adsorption at 273, 288 and 298 K (Fig. 4a). The simulated PXRD pattern was obtained from the single-crystal structure using the Mercury 2021.1.0 software, and the phase purity was determined through the as-synthesized sample. After activation treatments and CO_2 adsorption, the PXRD pattern was compared with the simulated PXRD pattern to check structure stability.

$[Zn_2(L)DMF]$ MOF showed that the thermal activation with vacuum evacuation at 120 °C caused a phase a slight crystalline loss or a phase transition. Supercritical CO_2 drying ($scCO_2$), a mild activation technique, was chosen to prove the amorphization. $scCO_2$ activation is based on avoiding the liquid-to-gas phase transition associated with capillary forces.[43] This activation has been successfully used for MOFs built from flexible linkers when conventional thermal activation causes the MOF's collapse or if the solvent exchange is unsuccessful.[44] However, after $scCO_2$ activation, a mixture of phases emerged, combining characteristics from both the "as-synthesized" and "activated at 120 °C" patterns.

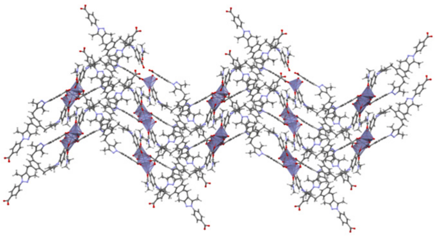

Fig. 3 3D view of the $[Zn_2(L)DMF]$.

Liu *et al.* reported that $scCO_2$ activation followed by conventional activation was highly effective in promoting the disruption of the coordination bond between the metal and the solvents that act as ligands, generating more efficient sites for CO_2 adsorption.[45]

The thermal stability of $[Zn_2(L)DMF]$ was evaluated by TGA (Fig. 4b). The initial weight loss over 270 °C can be attributed to the loss of DMF molecules coordinated to the Zn(II) in the nodes. Previous reports have demonstrated that DMF remained coordinated up to 260 °C in other MOFs.[46] The weight loss from 290 °C to 500 °C may be due to linker decomposition and collapse of the MOF structure. A plausible explanation for the temperature decomposition for the second and third events is the energy required to break different types of bonds. Benzene and pyrazole rings of the linker required lower energy than the coordinate bonds formed between the carboxylates and the zinc atoms. Also, breaking 14 Zn–O bonds in the node MOF is necessary.

The final remaining percentage of mass could be expected to be the node structure of the MOF. In this sense, the node $Zn_3(-COO)_6$ corresponds to ~23% of the whole network's weight. For previously reported trinuclear Zn-based MOFs, the decomposition temperature and residue percentage were over 400 °C and around 25%, respectively.[47]

Nitrogen (N_2) adsorption studies

The N_2 adsorption isotherm at 77 K up to 1 atm was measured on the $[Zn_2(L)DMF]$ sample. Previously, the MOF pores were fully evacuated by $scCO_2$ activation followed by thermal activation at 50 °C to remove possibly retained CO_2 molecules in the network. As can be observed in Fig. 5a, the N_2 adsorption isotherm on the activated sample resembles a typical type-I(a) isotherm according to the IUPAC classification,[48] typical for microporous materials. This profile indicates that at low rela-

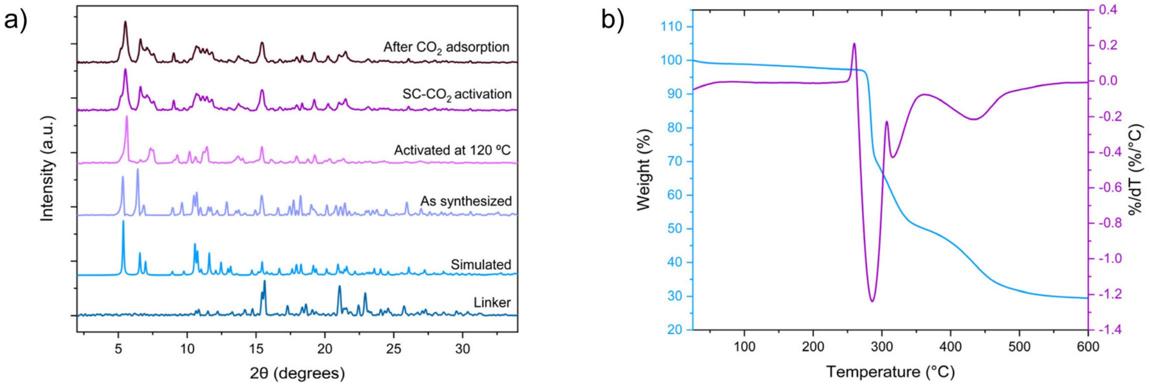

Fig. 4 For $[Zn_2(L)(DMF)]$. (a) PXRD patterns after several treatments. (b) TGA curve.

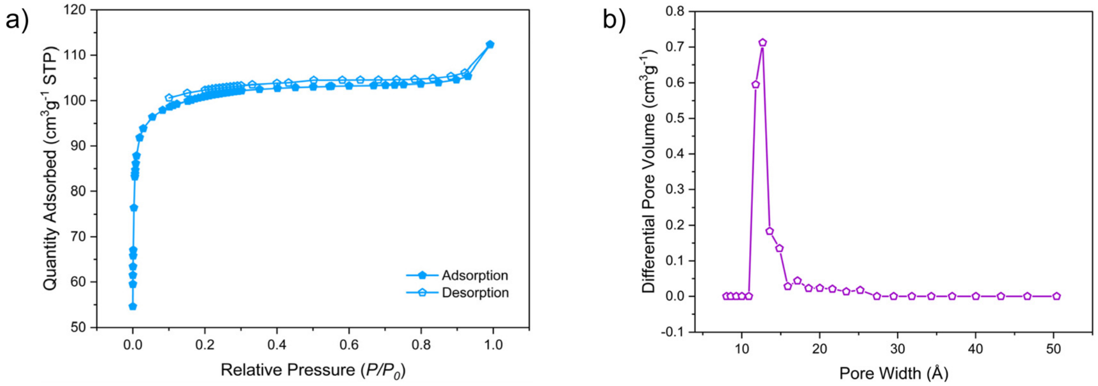

Fig. 5 (a) Nitrogen sorption isotherm at 77 K and (b) DFT calculated pore size distributions for [Zn_2(L)(DMF)].

tive pressure ($P/P^0 < 0.015$), the available micropores are occupied due to enhanced adsorbent–adsorptive interactions in narrow micropores, increasing substantially the quantity of N_2 adsorbed. The adsorbed gas quantity approaches a limiting value due to the lack of an external surface area rather than an internal surface area.[48,49] The BET surface area found was 402 m^2 g^{-1}. Furthermore, no hysteresis was observed upon desorption of gas from the pores. Fig. 5b shows the pore size distribution analysis based on DFT, which reveals a narrow distribution of micro-sized pores between 10–15 Å, with the maximum percentage at 12.5 Å. This result correlates well with the type of isotherm found.

CO_2 adsorption studies

In order to know the efficiency of the [Zn_2(L)DMF] MOF as CO_2 adsorber, the CO_2 sorption isotherms were measured from 0 to 75 kPa at 298 K, 288 K, and 273 K. The CO_2 uptake amounts were 3.0 wt% (15.41 cm^3 g^{-1}, 0.69 mmol g^{-1}), 4.2 wt% (21.60 cm^3 g^{-1}, 0.96 mmol g^{-1}), and 6.9 wt% (35.23 cm^3 g^{-1}, 1.57 mmol g^{-1}), respectively (see Fig. 6a). One or more of the following mechanisms could be responsible for the CO_2 adsorption in the MOF. First, CO_2 oxygen atoms may interact with hydrogens and metal atoms of the framework, particularly with coordinatively unsaturated metal centers or open metal sites (OMS). Second, the CO_2 carbon atom may be attracted to the negatively charged nitrogens of the pyrazole linkers.[17] It had been established that amine molecules and open nitrogen sites present high affinity toward CO_2 adsorption; thus pyrazole molecules act as Lewis basic sites and CO_2 molecules as the Lewis acids.[3] Finally, flexible and microporous MOFs are suitable for CO_2 adsorption.[50]

Comparable values, ranging between 16.67–35.84 cm^3 g^{-1} and 13.08–28.22 cm^3 g^{-1} at 273 K and 298 K, respectively, observed at 75 kPa have been reported for MOFs with structures based on a very similar flexible pyrazole carboxylate ligands, using triethylenediamine and 4,4-bipyridine as pillars.[51] These MOFs exhibit interpenetration and have a greater nitrogen content; however, the uptake values are not appreciably higher than those found here.

The interaction's strength between the framework and the CO_2 molecules was calculated by enthalpy of adsorption (ΔH_{ads}) by the Clausius Clapeyron equation at 273 K, 288 K, and 298 K. Before using the Clausius–Clapeyron approach, the isotherms at three temperatures must be fitted with the same continuous function. As most MOFs exhibit a Freundlich–Langmuir-type isotherm,[26] eqn (3) was used.

$$n = \frac{a \cdot b \cdot p^c}{1 + b \cdot p^c} \tag{3}$$

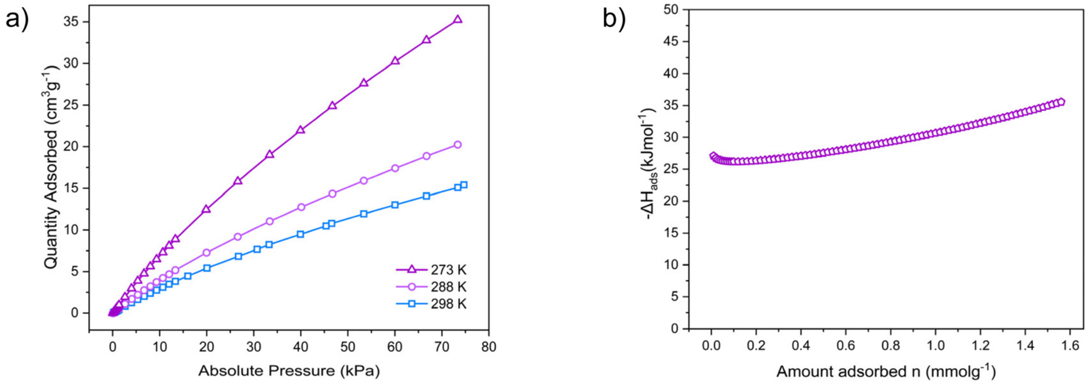

Fig. 6 For [Zn_2(L)(DMF)], (a) CO_2 adsorption isotherms at 273, 288 and 298 K, and (b) isosteric enthalpy of adsorption of CO_2.

Table 1 Morokuma–Ziegler EDA in kcal mol^{-1}

	ΔE_{Pauli}	ΔE_{Elec}	ΔE_{Orb}	ΔE_{Dis}	ΔE_{Int}	Atract	% elect	% orb	% dis
2 CO_2	23.0	−10.9	−5.2	−17.8	−10.8	−33.82	32	15	53
4 CO_2	45.1	−23.8	−9.6	−27.1	−15.5	−60.58	39	16	45
6 CO_2	75.0	−39.4	−16.3	−43.0	−23.8	−98.78	40	17	44
8 CO_2	107.0	−53.2	−23.9	−55.1	−25.1	−132.1	40	18	42

where n is the amount of CO_2 adsorbed (the loading) in mmol g^{-1}, p is the pressure in kPa, a is the maximal loading in mmol g^{-1}, b is the affinity constant (1/kPac), and c is the heterogeneity exponent. As shown in Fig. S19–S21,† the Freundlich–Langmuir fit with the obtained experimental data; therefore, the Clausius–Clapeyron equation can predict the ΔH_{ads}. The value for CO_2 at zero coverage was calculated to be 27 kJ mol^{-1} (Fig. 6b). As mentioned above, this value may be the average result of different types of interactions. Only the interaction between CO_2 and OMS sites accounts for the hybridization of the molecular orbitals, electrostatics, van der Waals forces, and Pauli repulsion.[3] The profile shows that ΔH_{ads} value slightly increases at higher pressures, which could be associated with intermolecular interaction between CO_2 molecules. On the other hand, at lower pressure, the adsorbate molecules are not close enough for an adequate interaction between them.[52] A quite similar ΔH_{ads} value (29.3–27.7 kJ mol^{-1}) was already reported for the MOF SNU-100′ ($[Zn_3(TCPT)_2(HCOO)][NH_2(CH_3)_2]$)[53] which has a trinuclear Zn node and nitrogen atoms in its structure similar to the herein report for the $[Zn_2(L)DMF]$ MOF.

Theoretical modelling

To account for the adsorption enthalpy and the interaction that CO_2 has with the MOFs, DFT calculations were performed over a reduced model of the MOFs pore. The studied model considers the portion of interest of the MOF that might be interacting with the CO_2. Therefore, two to eight CO_2 molecules were included in the cavity and beside it and allowed to arrive at a minimum over the potential energy surface.

As observed in Table 1, dispersion energy is the most important contribution to the CO_2–MOF interaction. The dispersion interaction comes from the attractive forces between the induced dipoles of the studied fragments. Its contribution to the attractive energies (in percentage) decreases as the number of CO_2 molecules increases. On the other hand, the second most important contribution of the interaction energy corresponds to the electrostatic interaction between the CO_2 molecules and the MOF cavity. Finally, as the number of CO_2 molecules increases inside the MOF cavity, the contribution of the orbital interaction percentage increases while the dispersion contrition percentage decreases. The increase in the orbital energy might be attributed to the increased number of molecule-molecule interactions, forcing them to overlap their electronic clouds. As shown in the ESI (see Fig. S22†), the CO_2 molecules show orbital interaction with the MOFs orbitals, which is shown in every calculated CO_2 representation. Finally, the fukui function of the empty MOF was plotted. As observed in the ESI (see Fig. S23†), the f− and the f+ are located over the linker's aromatic rings, which supports the reactivity of the CO_2 molecules over the aromatic rings.

Conclusion

In conclusion, a novel Zn(ɪɪ)-based metal–organic framework $[Zn_2(L)(DMF)]$ has been successfully synthesized *via* a solvothermal method by mixing a carboxylate pyrazole-based linker (L) and a Zn metal salt. This MOF comprises a trimetallic $Zn_3(-COO)_6(DMF)_2$ node coordinated to two linkers and two DMF molecules. Notably, the material exhibits a microporous crystalline structure, displaying an average pore diameter of 12.5 Å and a BET surface area of 402 m^2 g^{-1}. The intrinsic flexibility of the linker employed in the $[Zn_2(L)(DMF)]$ synthesis suggests that 'breathing' phenomena may be involved, giving attractive potential for gas adsorption applications. Notably, the recorded CO_2 uptake capacity reaches 35.23 cm^3 at 273 K, while the isosteric enthalpy of CO_2 adsorption stands at 27 kJ mol^{-1} at zero coverage.

Author contributions

All authors have given approval to the final version of the manuscript.

A. L.: Investigation, methodology, visualization, formal analysis, writing original draft. S. G.: Conceptualization, methodology, supervision. X. Z.: Investigation, formal analysis. E. S.: Investigation, formal analysis, resources, supervision, project administration. J. T. H.: Resources, supervision, project administration, funding acquisition.

Data availability

The data supporting this article have been included as part of the ESI.† Synthesis and characterization of the linker; crystal data and structure refinement for $[Zn_2(L)DMF]$; Freundlich–Langmuir fit for CO_2 adsorption isotherm on $[Zn_2(L)DMF]$ at different temperatures; and the molecular structure of the CO_2 interacting systems models.

Crystallographic data for the $[Zn_2(L)DMF]$ structure in CIF format has been deposited in the Cambridge Crystallographic Data Centre (CCDC) under deposition numbers CCDC 2355199.†

Conflicts of interest

The authors declare the following competing financial interest (s): J. T. H. has interest in NuMat Technologies, a company that commercializes MOFs.

Acknowledgements

This work was supported by ANID-Millennium Science Initiative Program-NCN2021_090. ANID/FONDAP/1523A0006. FONDECYT 1241917 and 1231194. ACT210057. FONDECYT Postdoctorado 3240504. At Northwestern, this work was supported by the U.S. Department of Energy, Office of Science, Basic Energy Sciences *via* grant DE-FG02-08ER15967.

References

1 A. Modak and S. Jana, Advancement in Porous Adsorbents for Post-Combustion CO_2 Capture, *Microporous Mesoporous Mater.*, 2019, **276**, 107–132, DOI: 10.1016/j.micromeso.2018.09.018.

2 J. M. Park, D. K. Yoo and S. H. Jhung, Selective CO_2 Adsorption over Functionalized Zr-Based Metal Organic Framework under Atmospheric or Lower Pressure: Contribution of Functional Groups to Adsorption, *Chem. Eng. J.*, 2020, **402**, 126254–125462, DOI: 10.1016/j.cej.2020.126254.

3 T. Ghanbari, F. Abnisa and W. M. A. Wan Daud, A Review on Production of Metal Organic Frameworks (MOF) for CO2 Adsorption, *Sci. Total Environ.*, 2020, **707**, 135090–135128, DOI: 10.1016/j.scitotenv.2019.135090.

4 C. Chen, M. Jia, G. Wang, X. Li and S. Li, High and Selective CO_2 Uptake in a Nitrogen-Rich Pillar-Layered Metal Organic Framework, *RSC Adv.*, 2015, **5**(127), 104932–104935, DOI: 10.1039/C5RA22144G.

5 A. Samanta, A. Zhao, G. K. H. Shimizu, P. Sarkar and R. Gupta, Post-Combustion CO_2 Capture Using Solid Sorbents: A Review, *Ind. Eng. Chem. Res.*, 2012, **51**(4), 1438–1463, DOI: 10.1021/ie200686q.

6 P. Muchan, C. Saiwan, J. Narku-Tetteh, R. Idem, T. Supap and P. Tontiwachwuthikul, Screening Tests of Aqueous Alkanolamine Solutions Based on Primary, Secondary, and Tertiary Structure for Blended Aqueous Amine Solution Selection in Post Combustion CO_2 Capture, *Chem. Eng. Sci.*, 2017, **170**, 574–582, DOI: 10.1016/j.ces.2017.02.031.

7 F. Bougie, D. Pokras and X. Fan, Novel Non-Aqueous MEA Solutions for CO_2 Capture, *Int. J. Greenhouse Gas Control*, 2019, **86**, 34–42, DOI: 10.1016/j.ijggc.2019.04.013.

8 P. Luis, Use of Monoethanolamine (MEA) for CO_2 Capture in a Global Scenario: Consequences and Alternatives, *Desalination*, 2016, **380**, 93–99, DOI: 10.1016/j.desal.2015.08.004.

9 Z. Du, X. Nie, S. Deng, L. Zhao, S. Li, Y. Zhang and J. Zhao, Comparative Analysis of Calculation Method of Adsorption Isosteric Heat: Case Study of CO_2 Capture Using MOFs, *Microporous Mesoporous Mater.*, 2020, **298**, 110053–100066, DOI: 10.1016/j.micromeso.2020.110053.

10 T. G. Grissom, D. M. Driscoll, D. Troya, N. S. Sapienza, P. M. Usov, A. J. Morris and J. R. Morris, Molecular-Level Insight into CO_2 Adsorption on the Zirconium-Based Metal–Organic Framework, UiO-66: A Combined Spectroscopic and Computational Approach, *J. Phys. Chem. C*, 2019, **123**(22), 13731–13738, DOI: 10.1021/acs.jpcc.9b02513.

11 V. Guillerm, D. Kim, J. F. Eubank, R. Luebke, X. Liu, K. Adil, M. S. Lah and M. Eddaoudi, A Supermolecular Building Approach for the Design and Construction of Metal–Organic Frameworks, *Chem. Soc. Rev.*, 2014, **43**(16), 6141–6172, DOI: 10.1039/C4CS00135D.

12 S. Li and F. Huo, Metal–Organic Framework Composites: From Fundamentals to Applications, *Nanoscale*, 2015, **7**(17), 7482–7501, DOI: 10.1039/C5NR00518C.

13 A. López-Periago, O. Vallcorba, C. Frontera, C. Domingo and J. A. Ayllón, Exploring a Novel Preparation Method of 1D Metal Organic Frameworks Based on Supercritical CO 2, *Dalton Trans.*, 2015, **44**(16), 7548–7553, DOI: 10.1039/C5DT00521C.

14 S. L. James, Metal-Organic Frameworks, *Chem. Soc. Rev.*, 2003, **32**(5), 276–288, DOI: 10.1039/b200393g.

15 V. V. Butova, M. A. Soldatov, A. A. Guda, K. A. Lomachenko and C. Lamberti, Metal-Organic Frameworks: Structure, Properties, Methods of Synthesis and Characterization, *Russ. Chem. Rev.*, 2016, **85**(3), 280–307, DOI: 10.1070/RCR4554.

16 H. Wang, Q.-L. Zhu, R. Zou and Q. Xu, Metal-Organic Frameworks for Energy Applications, *Chem*, 2017, **2**(1), 52–80, DOI: 10.1016/j.chempr.2016.12.002.

17 R. Poloni, K. Lee, R. F. Berger, B. Smit and J. B. Neaton, Understanding Trends in CO_2 Adsorption in Metal–Organic Frameworks with Open-Metal Sites, *J. Phys. Chem. Lett.*, 2014, **5**(5), 861–865, DOI: 10.1021/jz500202x.

18 D. Britt, H. Furukawa, B. Wang, T. G. Glover and O. M. Yaghi, Highly Efficient Separation of Carbon Dioxide by a Metal-Organic Framework Replete with Open Metal Sites, *Proc. Natl. Acad. Sci. U. S. A.*, 2009, **106**(49), 20637–20640, DOI: 10.1073/pnas.0909718106.

19 A. Lancheros, S. Goswami, X. Zarate, E. Blanco, E. Schott and J. T. Hupp, New Pillar-MOF with Nitrogen-Donor Sites for CO_2 Adsorption, *Cryst. Growth Des.*, 2024, **24**(14), 5898–5905, DOI: 10.1021/acs.cgd.3c01182.

20 H. A. Patel and C. T. Yavuz, Noninvasive Functionalization of Polymers of Intrinsic Microporosity for Enhanced CO_2 capture, *Chem. Commun.*, 2012, **48**(80), 9989–9991, DOI: 10.1039/c2cc35392j.

21 X. T. Liu, Y. Y. Jia, Y. H. Zhang, G. J. Ren, R. Feng, S. Y. Zhang, M. J. Zaworotko and X. H. Bu, A New Co(II) Metal-Organic Framework with Enhanced CO_2 Adsorption and Separation Performance, *Inorg. Chem. Front.*, 2016, **3**(12), 1510–1515, DOI: 10.1039/c6qi00191b.

22 S.-Y. Yu, Q. Jiao, S.-H. Li, H.-P. Huang, Y.-Z. Li, Y.-J. Pan, Y. Sei and K. Yamaguchi, Self-Assembly of Tripyrazolate-Linked Macrotricyclic $M_{12}L_4$ Cages with Dimetallic Clips, *Org. Lett.*, 2007, **9**(7), 1379–1382, DOI: **10.1021/ol070286d**.

23 O. V. Dolomanov, L. J. Bourhis, R. J. Gildea, J. A. K. Howard and H. Puschmann, OLEX2 : A Complete Structure Solution, Refinement and Analysis Program, *J. Appl. Crystallogr.*, 2009, **42**(2), 339–341, DOI: **10.1107/S0021889808042726**.

24 G. M. Sheldrick, SHELXT – Integrated Space-Group and Crystal-Structure Determination, *Acta Crystallogr., Sect. A: Found. Adv.*, 2015, **71**(1), 3–8, DOI: **10.1107/S2053273314026370**.

25 G. M. Sheldrick, A Short History of SHELX, *Acta Crystallogr., Sect. A: Found. Crystallogr.*, 2008, **64**(1), 112–122, DOI: **10.1107/S0108767307043930**.

26 A. Nuhnen and C. Janiak, A Practical Guide to Calculate the Isosteric Heat/Enthalpy of Adsorption via Adsorption Isotherms in Metal–Organic Frameworks, MOFs, *Dalton Trans.*, 2020, **49**(30), 10295–10307, DOI: **10.1039/D0DT01784A**.

27 E. J. Baerends, T. Ziegler, J. Autschbach, D. B. A. Bashford, F. M. Bickelhaupt, C. Bo, P. M. Boerrigter, L. D. P. Cavallo and L. Chong, *et al.*, *ADF2017, SCM, Theoretical Chemistry*, Vrije Universiteit, Amsterdam, The Netherlands, 2017, **https://www.Scm.com**.

28 G. te Velde, F. M. Bickelhaupt, E. J. Baerends, C. Fonseca Guerra, S. J. A. van Gisbergen, J. G. Snijders and T. Ziegler, Chemistry with ADF, *J. Comput. Chem.*, 2001, **22**(9), 931–967, DOI: **10.1002/jcc.1056**.

29 E. V. Lenthe, E. J. Baerends, J. G. Snijders, E. Lenthe, E. J. Van Baerends and J. G. Snijders, Relativistic Regular Twocomponent Hamiltonians Relativistic Regular Two-Component Hamiltonians, *J. Chem. Phys.*, 1993, **99**(6), 4597–4610, DOI: **10.1063/1.466059**.

30 E. van Lenthe, J. G. Snijders and E. J. Baerends, The Zero-Order Regular Approximation for Relativistic Effects: The Effect of Spin–Orbit Coupling in Closed Shell Molecules, *J. Chem. Phys.*, 1996, **105**(15), 6505–6516, DOI: **10.1063/1.472460**.

31 E. van Lenthe, E. J. Baerends and J. G. Snijders, Relativistic Total Energy Using Regular Approximations, *J. Chem. Phys.*, 1994, **101**(11), 9783–9792, DOI: **10.1063/1.467943**.

32 E. Van Lenthe and E. J. Baerends, Optimized Slater-Type Basis Sets for the Elements 1-118, *J. Comput. Chem.*, 2003, **24**(9), 1142–1156, DOI: **10.1002/jcc.10255**.

33 B. Hammer, L. B. Hansen and J. K. Nørskov, Improved Adsorption Energetics within Density-Functional Theory Using Revised Perdew-Burke-Ernzerhof Functionals, *Phys. Rev. B: Condens. Matter Mater. Phys.*, 1999, **59**(11), 7413–7421, DOI: **10.1103/PhysRevB.59.7413**.

34 S. Grimme, J. Antony, S. Ehrlich and H. Krieg, A Consistent and Accurate Ab Initio Parametrization of Density Functional Dispersion Correction (DFT-D) for the 94 Elements H-Pu, *J. Chem. Phys.*, 2010, **132**(15), 154104, DOI: **10.1063/1.3382344**.

35 L. Versluis and T. Ziegler, The Determination of Molecular Structures by Density Functional Theory. The Evaluation of Analytical Energy Gradients by Numerical Integration, *J. Chem. Phys.*, 1988, **88**(1), 322–328.

36 I. Cukrowski, J. H. De Lange and M. Mitoraj, Physical Nature of Interactions in ZnII Complexes with 2,2-Bipyridyl: Quantum Theory of Atoms in Molecules (QTAIM), Interacting Quantum Atoms (IQA), Noncovalent Interactions (NCI), and Extended Transition State Coupled with Natural Orbitals for Chemica, *J. Phys. Chem. A*, 2014, **118**(3), 623–637, DOI: **10.1021/jp410744x**.

37 H. Li, C. E. Davis, T. L. Groy, D. G. Kelley and O. M. Yaghi, Coordinatively Unsaturated Metal Centers in the Extended Porous Framework of $Zn_3(BDC)_3·6CH_3OH$ (BDC = 1,4-Benzenedicarboxylate), *J. Am. Chem. Soc.*, 1998, **120**(9), 2186–2187, DOI: **10.1021/ja974172g**.

38 M. Eddaoudi, H. Li and O. M. Yaghi, Highly Porous and Stable Metal–Organic Frameworks: Structure Design and Sorption Properties, *J. Am. Chem. Soc.*, 2000, **122**(7), 1391–1397, DOI: **10.1021/ja9933386**.

39 J. Liu, P. K. Thallapally, B. P. McGrail, D. R. Brown and J. Liu, Progress in Adsorption-Based CO_2 Capture by Metal–Organic Frameworks, *Chem. Soc. Rev.*, 2012, **41**(6), 2308–2322, DOI: **10.1039/C1CS15221A**.

40 W.-K. Wu and J.-L. Guo, Multifunctional Zinc Metal–Organic Framework for Highly Selective Detection of Picric Acid and Inhibition of Laryngeal Cancer Cell Growth, *J. Cluster Sci.*, 2020, **31**(2), 435–443, DOI: **10.1007/s10876-019-01657-x**.

41 Y.-L. Gan, K.-R. Huang, Y.-G. Li, D.-P. Qin, D.-M. Zhang, Z.-A. Zong and L.-S. Cui, Synthesis, Structure and Fluorescent Sensing for Nitrobenzene of a Zn-Based MOF, *J. Mol. Struct.*, 2021, **1223**, 129217–129223, DOI: **10.1016/j.molstruc.2020.129217**.

42 H.-F. Zhou, B. Liu, L. Hou, W.-Y. Zhang and Y.-Y. Wang, Rational Construction of a Stable Zn 4 O-Based MOF for Highly Efficient CO_2 Capture and Conversion, *Chem. Commun.*, 2018, **54**(5), 456–459, DOI: **10.1039/C7CC08473K**.

43 J. E. Mondloch, O. Karagiaridi, O. K. Farha and J. T. Hupp, Activation of Metal–Organic Framework Materials, *CrystEngComm*, 2013, **15**(45), 9258–9264, DOI: **10.1039/c3ce41232f**.

44 A. J. Howarth, A. W. Peters, N. A. Vermeulen, T. C. Wang, J. T. Hupp and O. K. Farha, Best Practices for the Synthesis, Activation, and Characterization of Metal–Organic Frameworks, *Chem. Mater.*, 2017, **29**(1), 26–39, DOI: **10.1021/acs.chemmater.6b02626**.

45 B. Liu, A. G. Wong-Foy and A. J. Matzger, Rapid and Enhanced Activation of Microporous Coordination Polymers by Flowing Supercritical CO_2, *Chem. Commun.*, 2013, **49**(14), 1419–1421, DOI: **10.1039/c2cc37793d**.

46 H. Alamgholiloo, S. Rostamnia, A. Hassankhani, J. Khalafy, M. M. Baradarani, G. Mahmoudi and X. Liu, Stepwise Post-Modification Immobilization of Palladium Schiff-Base Complex on to the OMS-Cu (BDC) Metal-Organic Framework for Mizoroki-Heck Cross-Coupling Reaction,

Appl. Organomet. Chem., 2018, **32**(11), e4539–e4548, DOI: **10.1002/aoc.4539**.

47 M. Xue, Z. Zhang, S. Xiang, Z. Jin, C. Liang, G.-S. Zhu, S.-L. Qiu and B. Chen, Selective Gas Adsorption within a Five-Connected Porous Metal–Organic Framework, *J. Mater. Chem.*, 2010, **20**(19), 3984–3988, DOI: **10.1039/b927486c**.

48 M. Thommes, K. Kaneko, A. V. Neimark, J. P. Olivier, F. Rodriguez-Reinoso, J. Rouquerol and K. S. W. Sing, Physisorption of Gases, with Special Rreference to the Evaluation of Surface Area and Pore Size Distribution (IUPAC Technical Report), *Pure Appl. Chem.*, 2015, **87**(9–10), 1051–1069, DOI: **10.1515/pac-2014-1117**.

49 K. A. Cychosz and M. Thommes, Progress in the Physisorption Characterization of Nanoporous Gas Storage Materials, *Engineering*, 2018, **4**(4), 559–566, DOI: **10.1016/j.eng.2018.06.001**.

50 Z. Chang, D. Yang, J. Xu, T. Hu and X. Bu, Flexible Metal–Organic Frameworks: Recent Advances and Potential Applications, *Adv. Mater.*, 2015, **27**(36), 5432–5441, DOI: **10.1002/adma.201501523**.

51 A. Lancheros, S. Goswami, M. R. Mian, X. Zhang, X. Zarate, E. Schott, O. K. Farha and J. T. Hupp, Modulation of CO_2 Adsorption in Novel Pillar-Layered MOFs Based on Carboxylate–Pyrazole Flexible Linker, *Dalton Trans.*, 2021, **50**(8), 2880–2890, DOI: **10.1039/D0DT03166F**.

52 S. Sircar and D. V. Cao, Heat of Adsorption, *Chem. Eng. Technol.*, 2002, **25**(10), 945–948, DOI: **10.1002/1521-4125(20021008)25:10<945::AID-CEAT945>3.0.CO;2-F**.

53 H. J. Park and M. P. Suh, Enhanced Isosteric Heat, Selectivity, and Uptake Capacity of CO_2 Adsorption in a Metal-Organic Framework by Impregnated Metal Ions, *Chem. Sci.*, 2013, **4**(2), 685–690, DOI: **10.1039/C2SC21253F**.